Receptivity of Hypersonic Boundary Layers to Distributed Roughness and Acoustic Disturbances

P. Balakumar

Flow Physics and Control Branch
NASA Langley research Center, Hampton, VA 23681.

Ponnampalam.balakumar-1@nasa.gov

ABSTRACT

Boundary-layer receptivity and stability of Mach 6 flow over smooth and rough 7° half-angle sharp-tipped cones are numerically investigated. The receptivity of the boundary layer to slow acoustic disturbances, fast acoustic disturbances, and vortical disturbances are considered. The effects of two-dimensional isolated and distributed roughness on the receptivity and stability are also simulated. The results show that the instability waves are generated in the leading edge region and that the boundary layer is much more receptive to slow acoustic waves than to the fast waves. Vortical disturbances also generate unstable second modes, however the receptivity coefficients are smaller than that of the slow acoustic wave. An isolated two-dimensional roughness element of height $h/\delta=1/4$ did not produce any difference in the receptivity or in the stability of the boundary layer. Distributed roughness elements produced a small decrease in the receptivity coefficient and also stabilized the boundary layer by small amounts.

1.0   INTRODUCTION

Transition from laminar to turbulent flow in hypersonic and supersonic boundary layers increases the skin friction and heat transfer on the vehicle[1]. The efficient design of a vehicle depends on predicting the transition fronts accurately and delaying the transition fronts using passive or active control methods. Transition in boundary layers occurs due to the growth of disturbances inside the boundary layer. These disturbances are initiated by free stream disturbances such as acoustic, turbulence, and other impurities in the free stream and/or by the surface nonuniformities such as roughness and surface vibrations. The evolution and breakdown of the disturbances inside the boundary layer depend on the initial amplitudes of the disturbances, flow parameters such as Mach number and Reynolds number, and the geometry of the vehicle. In quiet environments with small surface nonuniformities, the initial amplitudes of the disturbances are very small and the initial evolution of the disturbances occurs due to some linear instability mechanisms. These boundary-layer instabilities may include, but are not limited to, Tollmien-Schlichting, second-mode, attachment-line, and crossflow instabilities. In noisy environments with large surface roughness, the initial perturbations are large and the evolution bypasses the linear route and enters some nonlinear processes.

Transition in hypersonic boundary layers in quiet environments occurs due to the growth of unstable second mode disturbances inside the boundary layer[2, 3]. Numerical, experimental, and theoretical investigations have been performed to try to understand these instability modes for hypersonic boundary layers. Fedorov[4] recently reviewed the stability characteristics of hypersonic boundary layers. In previous work[5-9], the interactions of slow and fast acoustic waves, and vorticity waves with hypersonic boundary layers over sharp and blunt flat plates, wedges, and cones were investigated. The results show that flows over geometries with sharp leading

edges or tips produce instability waves that originate very close to the leading edge or tip and have receptivity coefficients about 5 to 10 times the amplitude of the forced slow acoustic wave. It was also found that the amplitude of the instability waves generated by the slow acoustic waves is about 20 times larger than that for fast acoustic waves. Vortical disturbances also generate unstable second modes and the amplitude of the instability mode is about 5 times smaller than that for the slow acoustic wave.

Surface roughness also affects the transition process in hypersonic boundary layers. Reda[10] and Schneider[11] reviewed the roughness-induced transition in hypersonic boundary layers. The surface roughness is characterized as either two-dimensional or three-dimensional, and either isolated or distributed. In addition to these global characteristics, local characteristics such as height, shape, and location of the roughness also influence the transition. Holloway et al.[12] and Fujii[13] experimentally observed that two-dimensional isolated roughness and a wavy wall delayed transition at hypersonic Mach numbers. Recently, Marxen et al.[14] numerically investigated the disturbance amplification in a Mach 4.8 flat plate boundary layer with localized two-dimensional roughness elements of different heights. Unsteady perturbations at a fixed frequency were generated by blowing and suction at the wall upstream of the roughness. They conclude that a two-dimensional roughness element acts like an amplifier capable of amplifying some frequency range and damping others. Bountin et al.[15] investigated experimentally and numerically the control of the second mode waves using a spanwise corrugated surface at a Mach number of 6. The results showed that the separation bubbles formed between the grooves stabilize the growth of the second modes. In their simulation, the unsteady perturbations are also introduced by the blowing and suction on the wall. However, questions remain about the role of the roughness in the generation and growth of the second modes generated by the free stream disturbances. Does the roughness affect the receptivity process of the second modes generated by the free stream acoustic and vortical disturbances and/or does the roughness modify the boundary layer downstream and hence modify the stability characteristics? The work presented in this paper is aimed at answering these questions.

The focus of this paper is on the effects of two-dimensional isolated and distributed roughness located near the nose region on the generation and evolution of second mode disturbances in hypersonic boundary layers. The effects of two-dimensional roughness in hypersonic boundary layers over a 7° half-angle sharp-tipped cone at a free stream Mach number of 6 are investigated. First, the disturbance field generated by the interaction of free stream slow acoustic waves, fast acoustic waves, and vorticity waves with the smooth cone is simulated. Then, rectangular shaped two-dimensional isolated and distributed roughness are placed near the nose region and the simulation is performed to study the effects of the roughness on the receptivity and the stability.

2.0   MODELS AND FLOW CONDITIONS

The model is a 7° half-angle sharp-tipped cone with a nose radius of 0.015 mm (Fig. 1a). Computations were performed for a freestream Mach number of 6. The freestream stagnation temperature and pressure were 433°K and 12.2 kPa (140 psi), yielding a unit Reynolds number of $10.4*10^6$/m. The simulations were performed for a constant wall temperature of 300°K. The cone model geometry was tested in the Boeing/AFOSR Mach 6 Quiet Tunnel at the same freestream conditions.[16] The Sutherland viscosity law was used with a constant Prandtl number of 0.70. The non-dimensional frequency F is defined as $F = \dfrac{2\pi\nu_\infty f}{U_\infty^2}$, where f is the frequency in hertz. For the above flow conditions, $F = 1*10^{-4}$ corresponds to a frequency of 144.23 kHz**.**

1.1   Roughness

Two-dimensional roughness elements were placed on the surface of the cone at different locations along the cone. The shape of the roughness is in the form

$$y_c(x) = \frac{h}{2} \sum_{n=1}^{N} \left[\tanh \sigma \frac{x - x_n}{\Delta x} - \tanh \sigma \frac{x - (x_n + w)}{\Delta x} \right]$$

$$x_n = x_0 + (n-1)*(2w)$$

(1)

Here y_c is the height of the roughness normal to the surface of the cone, h is the maximum height, x_o is the starting location of the roughness, w is the width of the roughness, σ and Δx determine the spatial extent of the roughness near the edge. The spacing between two roughness elements in the simulations is two times the width of one roughness. "N" is the number of roughness elements. Fig. 1(b) depicts the shape for an isolated roughness and Fig. 1(c) shows the roughness distribution for multiple roughnesses. These patterns resemble the steps and gaps formed by the movement of the surface tiles. Simulations are performed for different widths, heights, locations, and number of roughness elements.

2.0   GOVERNING EQUATIONS

The two-dimensional unsteady compressible Navier-Stokes equations are solved, written in conservation form and in cylindrical coordinates. The governing equations were solved using a 5th-order accurate weighted essentially non-oscillatory (WENO) scheme for space discretization and a 3rd-order total-variation-diminishing (TVD) Runge-Kutta scheme for time integration. The solution method implemented in the present computations is described in Kara et al[5].

A body-fitted curvilinear grid system was used in all simulations. The grid stretches in the normal direction close to the wall and is uniform outside of the boundary layer. In the x direction, the grid was very fine near the nose and over the roughness and then uniform in the region downstream. The outer boundary that lies outside of the shock follows a parabola with its vertex located a short distance upstream of the leading edge of the plate. The computational domain extends from $x = -0.001$ to 0.55 meters in the axial direction. This gives a maximum Reynolds number of $Re = 2280.0$ at the end of the computational domain. Calculations were performed using grid sizes of 7001*251 and 10001*251.

3.0   RESULTS

3.1   Meanflow and Linear Stability without Roughness

Figure 2(a) and (b) show the computed mean density contours for the sharp-tipped cone. The flow field for the entire computational domain is shown in Fig. 2(a), while Fig. 2(b) shows a close-up view of the nose region. The mean flow boundary layer profiles at different axial locations $x = 0.5, 3, 10, 20, 30$ and 50 cm are shown in Fig. 3. The boundary layer thickness increases from 0.20 mm at $x = 0.5$ cm. to 2.0 mm at $x = 50$ cm. Linear stability results are shown in Figs. 4 and 5. Figure 4 shows the N-Factor variation for different frequencies obtained using parallel and non-parallel PSE methods. The maximum N-factor obtained is about 7.0 and the corresponding frequency is $F=1.5*10^{-4}$ (220 kHz).

Figs. 5(a) and 5(b) show the evolution of the eigenvalues along the axial direction for the slow (Mode S) and fast (Mode F) modes for the frequency $F = 1.5*10^{-4}$. Figure 5(a) shows the evolution of phase speed c_r and the

growth rate $-\alpha_i$ and Fig. 5(b) shows the wavenumber α_r and the wavelength. As the fast mode evolves downstream, it merges with the continuous spectrum with phase speed $c_r = 1.0$. For this frequency of $F = 1.5*10^{-4}$ the merging occurs around $x = 281$ mm. Downstream of the continuous spectrum a new mode with slightly different eigenvalues and eigenfunctions emerges. These points are also marked as red dots in Fig. 5(a). As the slow mode and the new fast mode evolve downstream, the slow mode becomes the unstable Mack's second mode and the fast mode becomes the stable mode. The synchronization of the phase speeds for the slow and the fast modes occurs near $x = 360$ mm. The growth rates of the slow mode and the fast mode at this point are $-\alpha_i = 0.005$ and -0.02, respectively. The continuous spectrum and the synchronization point are also marked as vertical lines in Figs 5(a) and (b), respectfully. This figure suggests that roughness located near the nose, the continuous spectrum location, and the synchronization region may influence the receptivity of the unstable second mode.

Table 1 gives the wavenumbers and the wavelengths in dimensional and non-dimensional units for the slow and the fast acoustic waves, the vorticity waves, and for the neutral stability waves. It is interesting to see that in all the cases the wavelengths for the acoustic waves match with the wavelengths for the stability waves. The wavelengths of the slow and the fast acoustic waves at zero incidence at the frequency $F = 1.50*10^{-4}$ are 3.35 and 4.69 mm, and the wavelengths for the slow and the fast instability waves near the leading edge of the cone are 3.47 and 4.64 mm. The wavelengths of the vorticity waves do not match the wavelengths of either the slow or the fast modes. The wavelength of the vorticity wave is 4.02 mm, which lies in the middle of the wavelengths for the slow and the fast stability modes.

Table 1: Values of α_{ac} and wavelength at the frequency of $F = 1.5*10^{-4}$.

θ_y	Slow acoustic	Fast acoustic	Vorticity	Cone (Stability) X=60mm	
				Slow	Fast
0	0.1835 (3.35 mm)	0.1310 (4.69 mm)	0.153 (4.02 mm)	0.1772 (3.47 mm)	0.1328 (4.64 mm)

3.2 Interaction of Slow, Fast Acoustic Waves and Vorticity Waves with the Cone without the Roughness

Detailed results for the interactions of slow acoustic waves, fast acoustic waves, and vorticity waves are given in a previous paper[9]. After the mean flow was computed, two-dimensional slow and fast acoustic disturbances and vorticity disturbances (with an amplitude of $\tilde{p}_{ac}/p_\infty = 1*10^{-5}$ for the acoustic waves and with an amplitude of $\tilde{u}/U_\infty = 1.0*10^{-5}$ for the vorticity waves) at an incidence angle of 0 degrees were introduced at the outer boundary of the computational domain and time-accurate simulations were performed. The results are presented for the most amplified frequency of $F = 1.5*10^{-4}$ (217 kHz). Contours of the density fluctuations generated by the slow acoustic waves are shown in Fig. 6(a) for the nose region, and in Fig. 6(b) for the tip region. For the slow mode, the acoustic waves are very weakly transmitted through the shock. It is also observed that the fluctuations inside the boundary layer are larger than the amplitude of the incoming acoustic field. It suggests that the boundary layer is perturbed strongly starting from the nose region. The fast acoustic mode is transmitted strongly across the shock as compared to the slow mode case. The perturbations inside the boundary layer are larger than the amplitude of the incoming wave. Fig. 6(d) also shows that the amplitude inside the boundary layer does not increase or decrease uniformly. In some regions it increases and in some

regions it decreases to very small values.

Figures 7(a-c) show the amplitude of the pressure fluctuations along the surface of the cone for the slow and the fast acoustic waves and for the vorticity waves. Figure 7 also includes the results from the parabolized stability equations (PSE) computations obtained for the same mean boundary layer profiles. The figure for the slow wave clearly shows the initial generation and the eventual exponential growth of the instability waves inside the boundary layer. The slow acoustic wave whose wavelength (3.35 mm) is close to the wavelength of the slow mode (Mode S) near the leading edge (3.47 mm) transforms into instability waves rather directly. Similarly, the fast acoustic mode whose wavelength (4.69 mm) is close to the wavelength of the fast mode (Mode F) near the leading edge (4.64 mm) synchronizes with the instability mode near the leading edge region. As was observed in Fig. 5(a), the fast mode does not evolve into an unstable second mode as the Reynolds number increases. Figure 7(b) shows that as the disturbance induced by the fast mode evolves downstream it first grows up to $x \sim 12$ cm, then decreases and oscillates before it grows due to the second mode instability. The unstable second mode generated by the fast mode is weak compared to that generated by the slow mode. The maximum amplitude reached in the slow acoustic wave case is about 0.213 and it is about 0.0023 in the fast acoustic case.

Table 2: Maximum amplitudes of pressure fluctuations for different cases F=1.5*10^{-4}

θ_y	Max. amplitude	Ratio =max /max$_{slow}$
0 *Slow*	0.213	1.0
0 *Fast*	0.0023	1/93
0 Vorticity	0.078	1/2.7

Simulations were also performed with axisymmetric vortical disturbances.[9] Figures 7(c) depicts the wall pressure fluctuations generated by the interaction of vortical disturbances with the cone. The results show that the disturbances grow up to $x \sim 30$ cm, then decrease to a minimum value close to $x = 33$ cm and increase downstream due to the second mode instability. The maximum amplitude obtained in this case is about 0.078. Table 2 summarizes the maximum amplitudes reached by the disturbances in different cases. The fast mode is about 93 times less efficient than the slow mode, and the vortical disturbance is about 2.7 times less efficient.

3.3   Mean Flow with Roughness

3.3.1   Isolated roughness

First, the mean flow profiles obtained with an isolated roughness are presented. The roughness is located at x_0 = 5 mm and the width of the roughness is $w = 1.25$ mm. The simulations are performed for the roughness

heights of $h = 0.05$ and 0.10 mm. The boundary layer thickness at $x = 5.0$ mm is about 0.20 mm. The heights of the roughness in terms of the boundary layer thickness are $h/\delta = 1/4$ and 1/2 respectively. The roughness Reynolds number, Re_{kk}, based on the flow variables at the roughness height and at $x = 5$ mm are 13 and 106 for the roughness heights $h/\delta = 1/4$ and 1/2 respectively. Figure 8(a) shows the density contours very close to the roughness. The figure shows the compression waves formed in front and back of the roughness element. The compression wave formed in front of the roughness is stronger than that at the trailing edge. The compression wave intersects the main shock and deflects the main shock slightly. The compression wave at the trailing edge is at a smaller angle and merges with the main shock further downstream. Figures 9(a) and (b) depict the streamline patterns over the roughness for the roughness heights $h = 0.05$ and 0.10 mm, respectively. At smaller roughness, the streamlines follow the roughness without significant separation. At the larger roughness case, $h = 0.10$ mm, the flow separates upstream and downstream of the roughness. The flow separates at $x = 4.6$ mm in the front of the roughness and attaches below the crest. The length of the separation bubble is about $4h$. The flow separates at the trailing edge of the crest and reattaches at $x = 6.35$ mm. The length of the bubble is about $1h$. Figure 10(a) shows the surface pressure distribution obtained with and without the roughness for the two roughness heights $h = 0.05$ and 0.10 mm. The figure clearly shows the strong pressure rise in front of the roughness, followed by an over expansion over the roughness and recompression near the trailing edge of the roughness. Figure 11 shows the variation of the amplitude of the pressure fluctuations along the wall computed using the non-parallel PSE method for the mean flows obtained with and without roughness. The stability calculations show that the isolated roughness height of $h/\delta = 1/4$ did not produce any noticeable difference in the stability of the boundary layer.

3.3.2   Distributed roughness

Similar to the single roughness case, Figs. 8(b), 9(c) and 10(b) display the density contours, streamlines over the roughness, and the pressure distributions along the distributed roughness, respectively. The roughness shape and the distribution are given in eq. (1). The results are presented for the case with $h = 0.10$ mm, $w = 1.25$ mm, and N = 40. The distributed roughness spans from $x = 5$ mm to $x = 105$ mm. The distance between two roughness is 2.5 mm. The results first show that as the boundary layer evolves over the roughness a pattern of compression, expansion, and another compression wave is formed over each element. However, the strength of these waves decreases with successive roughness. It is also observed that there exists a strong expansion and a compression at the end of the roughness $x \sim 105$ mm (Fig. 10(b)) before the pressure recovers back to the unperturbed pressure. Hence at the trailing edge there exists an adverse pressure gradient. This may in some cases make the flow separate downstream of the roughness. Similar to the single roughness case, the flow separates upstream and downstream of roughness. However, the upstream separation bubble becomes smaller for downstream roughness and by $x \sim 61.5$ mm (near the 25th roughness element), the flow does not separate ahead of the roughness. The downstream separation bubble becomes stronger. At the end of the distributed roughness the trailing-edge separation bubble length is about 3h. Figure 11 shows the stability computations performed using the PSE method. The results show that the roughness stabilized the downstream boundary layer. The maximum amplitudes decrease by factors of 1.2 and 1.4 times from the smooth cone case for the roughness heights of $h/\delta = 1/4$ and 1/2 respectively.

3.4   Interaction of Slow, Fast Acoustic Waves and Vorticity Waves with an Isolated Roughness

After computing the mean flow, two-dimensional slow/fast acoustic disturbances $\tilde{p}_{ac}/p_\infty = 1*10^{-6}$ and vorticity disturbances $\tilde{u}/U_\infty = 1*10^{-6}$ at an incidence angle of 0 degrees were introduced at the outer boundary of the computational domain and time-accurate simulations were performed. The results are presented for a

frequency of $F = 1.5*10^{-4}$ (217 kHz) and with $h = 0.05$mm, $w = 1.25$ mm. Contours of the density fluctuations over the roughness generated by the interactions are shown in Figs. 12(a-c). The slow acoustic wave generates the unstable eigenmodes near the nose region. After that, the waves evolve downstream determined by the characteristics of the boundary layer. The figures show that well organized disturbances approach the roughness element from upstream and transmit through the compression waves unmodulated. The wavelength of the disturbances in this case is about 2.7 times longer than the width of the roughness. A parametric study increasing the width and height of the roughness is needed to see whether this conclusion remains the same. Figures 13(a-c) show the wall pressure fluctuations generated by the interactions for all three cases. Also included are the results obtained in the smooth case. It is seen that there are no differences in the amplitudes of the disturbances downstream of the roughness in all the cases. Hence for these parameters, $h/\delta = 1/4$, the roughness does not influence the receptivity of the disturbances generated by the free stream acoustic and vortical disturbances.

3.5   Interaction of Slow, Fast Acoustic Waves and Vorticity Waves with Distributed Roughness

Similar to the previous isolated roughness case, simulations are performed with multiple roughness elements. The results are presented for the interaction of a slow acoustic wave with the roughness cases $h = 0.05$ and 0.10 mm with $w = 1.25$ mm, N = 40. Figure 14 shows the contours of the density fluctuations generated by the interaction over the roughness elements. Notice that the perturbations are located at the edge of the boundary layer. Qualitatively, the picture conveys that roughness does not influence the structure of the disturbances. The structures evolve on top of the roughness elements without much deformation. Figures 15 and 16 give the quantitative comparison of the wall pressure fluctuations generated by the interaction of a slow acoustic wave with a smooth and a rough cone. Figure 15 depicts the results very close to the roughness and Fig. 16 depicts the results for the entire domain. Figures 15(a) and 16(a) show the results for the roughness height $h = 0.05$ mm and Figs. 15(b) and 16(b) show the results for the case $h = 0.10$ mm. Downstream of the roughness elements, $x \sim 105$ mm, the amplitudes of the disturbances are smaller for the cases with the roughness compared to that without the roughness. This reduction increases with the height of the roughness. The maximum pressure fluctuations amplitude ratios without and with the roughness are about 1.35 and 1.95 for the roughness heights $h = 0.05$ and 0.10 mm, respectively. Figure 11 showed that the amplitude reductions due to the stability part are 1.2 and 1.4 for these two roughnesses. Hence, receptivity of the instabilities, downstream of the roughness decreased by factors of 1.1 and 1.4 due to the distributed roughness heights $h = 0.05$ and 0.10 mm, respectively. This shows that a series of roughness elements reduces the receptivity coefficients of the instability waves generated by the free stream disturbances and also stabilizes the downstream boundary layer. However, these effects are small to have an influence on the transition induced by the second modes.

4.0   CONCLUSIONS

The receptivity of the instability waves to two-dimensional acoustic and vortical waves in hypersonic flows over a sharp-tipped a cone at a free stream Mach number of 6 and at a Reynolds number of $10.4*10^6$/meter was numerically investigated. The effects of two-dimensional isolated and distributed roughness elements located in the nose region on the receptivity and stability of the boundary layer was also studied. Both the steady and unsteady solutions were obtained by solving the compressible Navier-Stokes equations using the 5th-order accurate weighted essentially non-oscillatory (WENO) scheme for space discretization and using a third-order total-variation-diminishing (TVD) Runge-Kutta scheme for time integration. In the smooth cone case, the receptivity coefficient for the slow mode is about 5 times the amplitude of the freestream slow

acoustic wave. It was also found that the amplitude of the instability waves generated by the slow acoustic waves is about ninety times larger than that for the case of fast acoustic waves. This also illustrates the importance of the slow acoustic wave compared to the fast wave in causing transition in adiabatic hypersonic boundary layers. Axisymmetric vortical disturbances also generate unstable second modes in hypersonic boundary layers. The receptivity coefficient is about three times smaller than that for the slow acoustic wave.

The isolated roughness element of height $h/\delta = 1/4$ located near the nose region did not influence the receptivity or the stability of the boundary layers. The disturbances generated by the free stream acoustic and vortical disturbances reside at the edge of the boundary layer and convect over the roughness without any modulation. Even the strong compression waves formed at the front and back of the roughness did not influence the amplitude of the disturbances. Increasing the height of the roughness will, however, eventually influence the stability characteristics of the boundary layer. The distributed roughness elements produced a small decrease in the receptivity coefficient of the instability waves generated by the slow acoustic wave. The results also showed that the boundary layer downstream of the roughness becomes more stable compared to the smooth cone case. However, these effects are small. The effects of the roughness location on the receptivity and stability of the boundary layer still need to be studied. These questions will be considered in future work.

5.0   REFERENCES

[1]   Horvath, T. J., Berry, S. A., and Merski, N. R., "Hypersonic Boundary/Shear Layer Transition for Blunt to Slender Configurations: a NASA Langley Experimental Perspective.," RTO-MP-AVT_111, Art. 22. 2004.

[2]   Mack L., "Boundary Layer Stability Theory," JPL Report No. 900-277 Rev. A, Pasadena, Calif, Nov. 1969.

[3]   Kendall,J. M., "Wind Tunnel Experiments Relating to Supersonic and Hypersonic Boundary-Layer Transition," *AIAA J.,* Vol. 13, No. 3, 1975, pp. 290-299.

[4]   Fedorov, A. V., "Transition and Stability of High-Speed Boundary Layers," Annu. Rev. Fluid Mechanics, 2011. 43:79-95.

[5]   Kara, K. Balakumar, P. and Kandil, O. A., "Effects of Nose Bluntness on Hypersonic Boundary Layer Receptivity and Stability over Cones," AIAA Journal, Vol. 49, No. 12, December 2011, pp. 2593-2606.

[6]   Kara, K., Balakumar, P., and Kandil, O.A., "Effects of Nose Bluntness on Stability of Hypersonic Boundary Layers over a Blunt Cone," AIAA Paper 2007-4492, June 2007.

[7]   Kara, K., Balakumar, P., and Kandil, O.A., "Effects of Wall Cooling on Hypersonic Boundary Layer Receptivity over a Cone," AIAA Paper 2008-3734, June 2008.

[8]   Balakumar, P., and Kegerise, M. A., "Receptivity of Hypersonic Boundary Layers over Straight and Flared Cones," AIAA Paper 2010-1545, January 2010.

[9]   P. Balakumar, and Kegerise, M. K., "Receptivity of Hypersonic Boundary Layers to Acoustic and Vortical Disturbances," AIAA 2011-0371, 49th AIAA Aerosciences Meeting, Orlando, Florida, January

4-7, 2011.

[10] Reda, D. C., "Review and Synthesis of Roughness-Dominated Transition Correlations for Reentry Applications," J. Spacecraft and Rockets 39 2:161-167.

[11] Schneider, S. P., "Summary of Hypersonic Boundary-Layer Transition Experiments on Blunt Bodies with Roughness," J. Spacecraft and Rockets 45 6:1090-1105.

[12] Holloway, P., and Sterett, J., "Effect of Controlled Surface Roughness on Boundary-Layer Transition and Heat Transfer at Mach Numbers of 4.8 and 6.0," NASA, TR TN D-2054, 1964.

[13] Fujii, K. "Experiment of the Two-Dimensional Roughness effect on Hypersonic Boundary-Layer Transition," Journal of Spacecraft and Rockets, Vol.43, No. 4, July-August 2006.

[14] Marxen, O., Iaccarino, G., and Shaqfeh, E. S., "Disturbance Evolution in a Mach 4.8 Boundary Layer with Two-Dimensional Roughness-Induced Separation and Shock," J. Fluid Mech. (2010). Vol. 648, pp. 435-469.

[15] Bountin, D., Chimitov, T., Maslov, A., Novikov, A., Egorov. I, and Fedorov, A., "Stabilization of a Hypersonic Boundary Layer using a Wavy Surface," AIAA-2012-1105, January 2012.

[16] Wheaton, B., Juliano, T.J., Berridge, D.C., Chou, A., Gilbert, P.L., Casper, K.M., Steen, L.E., Schneider, S., and Johnson, H.B., "Instability and Transition Measurements in the Mach 6 Quiet Tunnel," AIAA Paper 2009-3559, June 2009.

Receptivity of Hypersonic Boundary Layers to
Distributed Roughness and Acoustic Disturbances

(a)

$$p_{ac} = a\ exp(\ i\ (\alpha_{ac}x \pm \beta_{ac}z + \varepsilon_{ac}y - \omega t)) + c.c$$

$\theta = 90$

r

$\theta = 0$

$M = 6.0$

θ_c

Outer boundary

Cone

r_0

$M_\infty = 6.0$

$Re = 10.4*10^6\ /m$

$T_0 = 433°\ K$

$T_\infty = 52.43°\ K$

$T_{wall} = 300.0°\ K$

Nose radius $r_0 = 0.015$ mm

Cone half-angle = 7 degrees.

(b)

w

$x = x_o$

h

(c)

$2w$
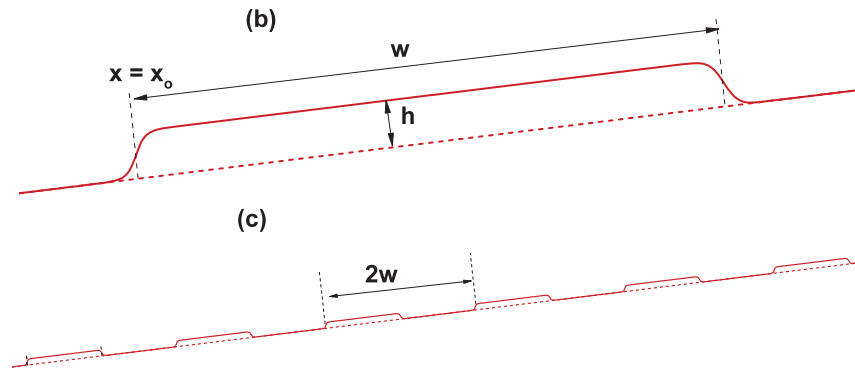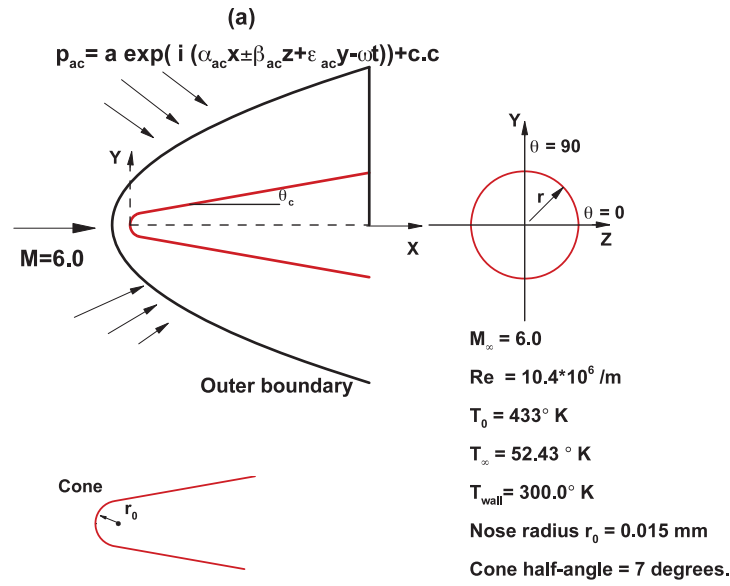
Figure 1: Schematic diagram of the model for flow over (a) a 7-degree sharp-tipped cone (b) shape of a single roughness (c) configuration of multiple roughness.
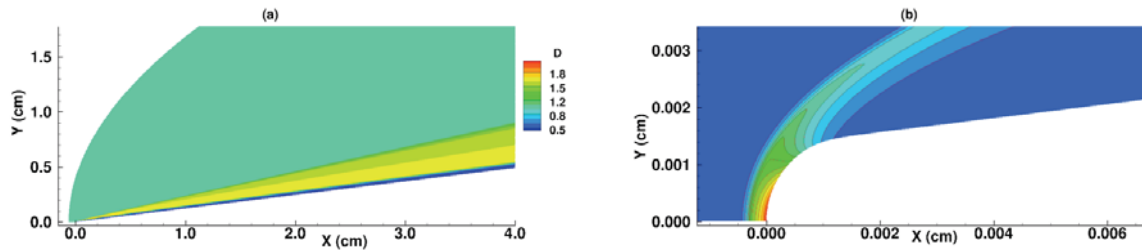
Figure 2: Mean density contours for flow over a 7-degree cone without roughness at Mach 6.
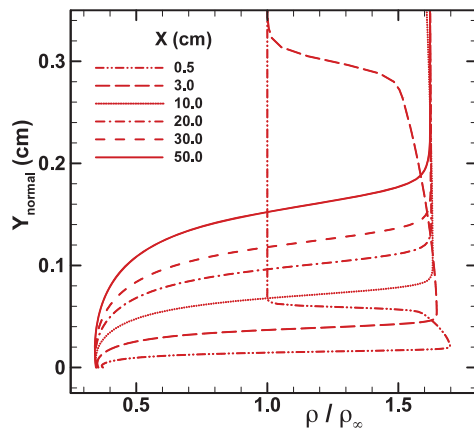
Figure 3: Boundary layer density profiles at different axial locations without roughness.
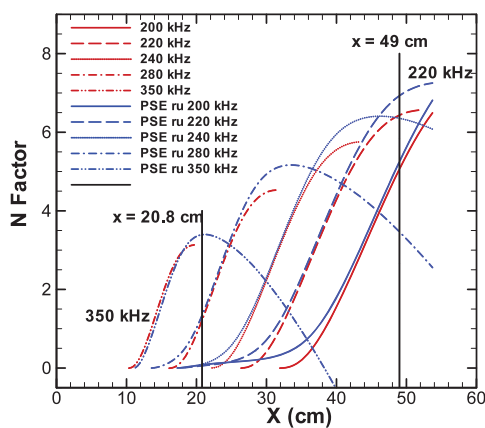
**Figure 4: N-Factor curves computed from the linear stability analysis and the PSE analysis based on
$(\rho u)_{max}$.**

Receptivity of Hypersonic Boundary Layers to
Distributed Roughness and Acoustic Disturbances
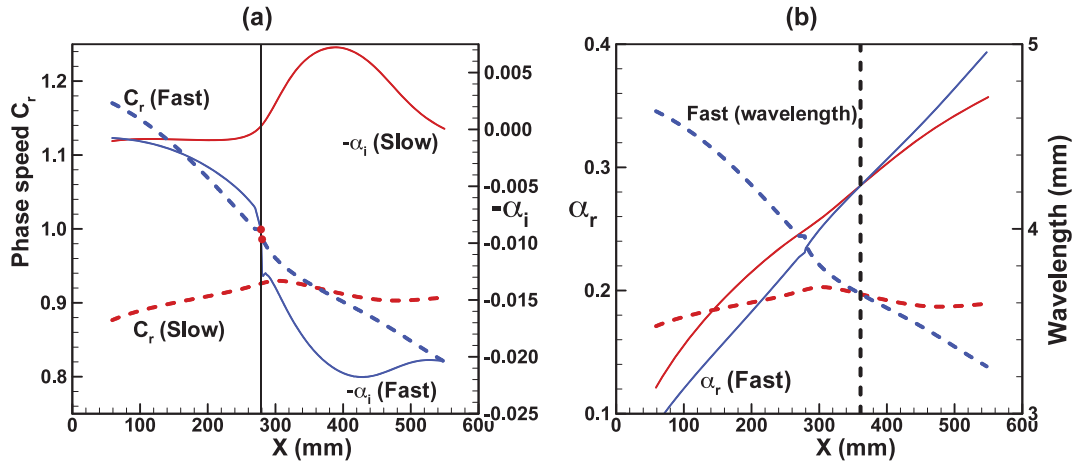
Figure 5: Eigenvalues from the linear stability computations for fast (blue) and slow (red) modes for the frequency $F=1.5*10^{-4}$. (a) Phase speed c_r and growth rates $-\alpha_i$ and (b) wavenumber α_r and wavelength.
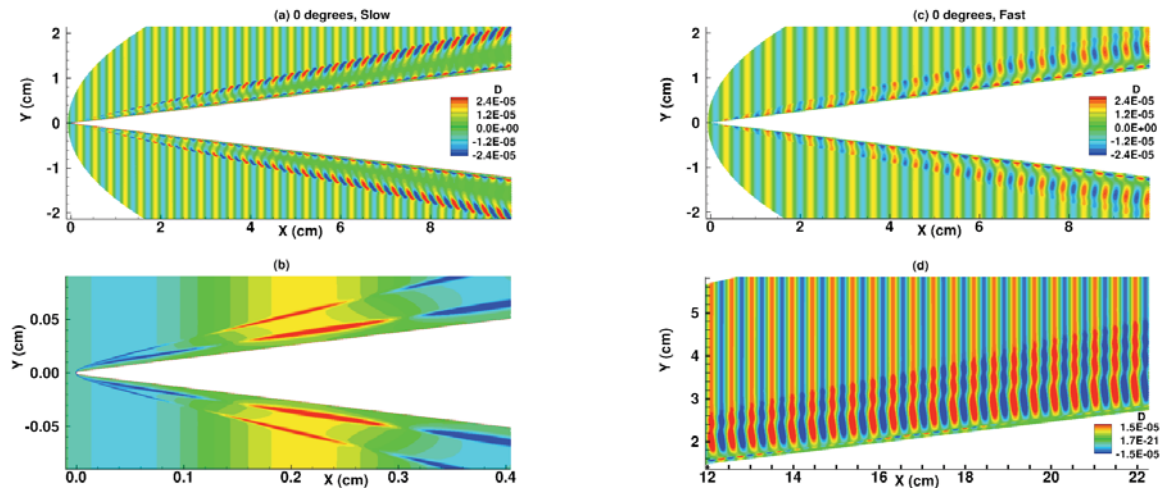
Figure 6: Density fluctuations generated by the interaction of two-dimensional plane slow and fast acoustic waves without roughness. $F=1.5*10^{-4}$.
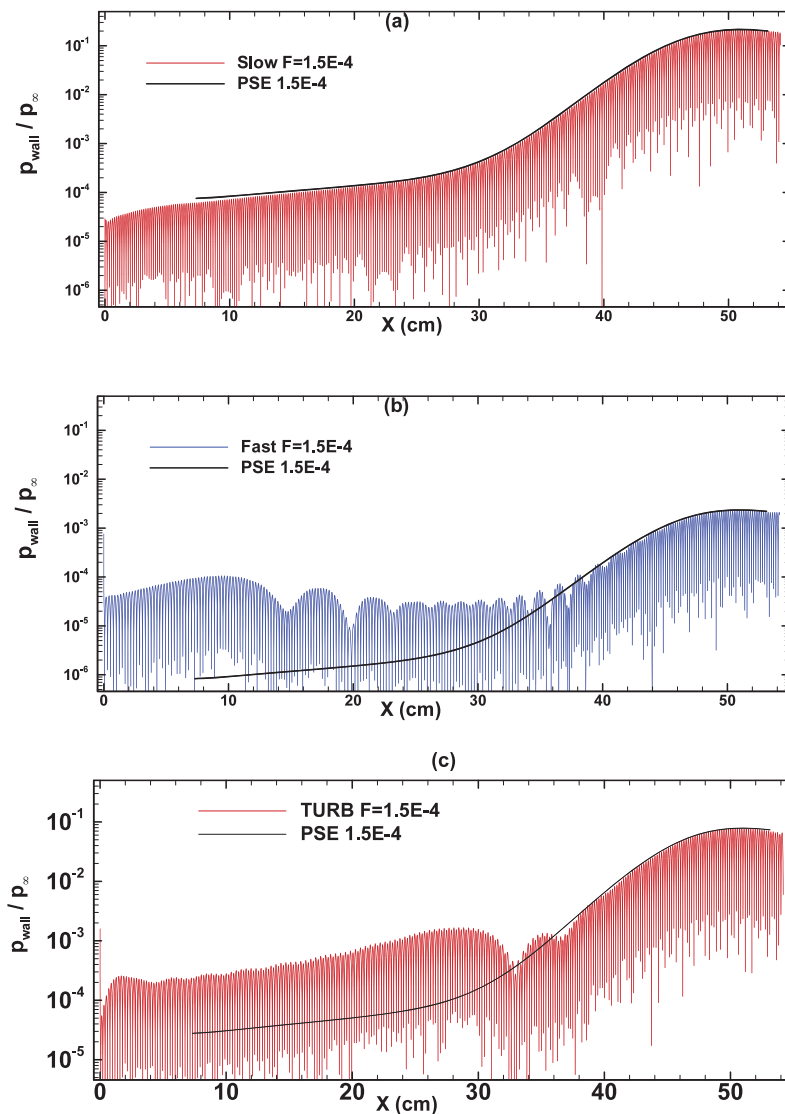
**Figure 7: Wall pressure fluctuations generated by the interaction of (a) a two-dimensional slow
acoustic wave (b) a fast acoustic wave and (c) an axi-symmetric vortical disturbances without
roughness in log-scale.** $F=1.5*10^{-4}$.
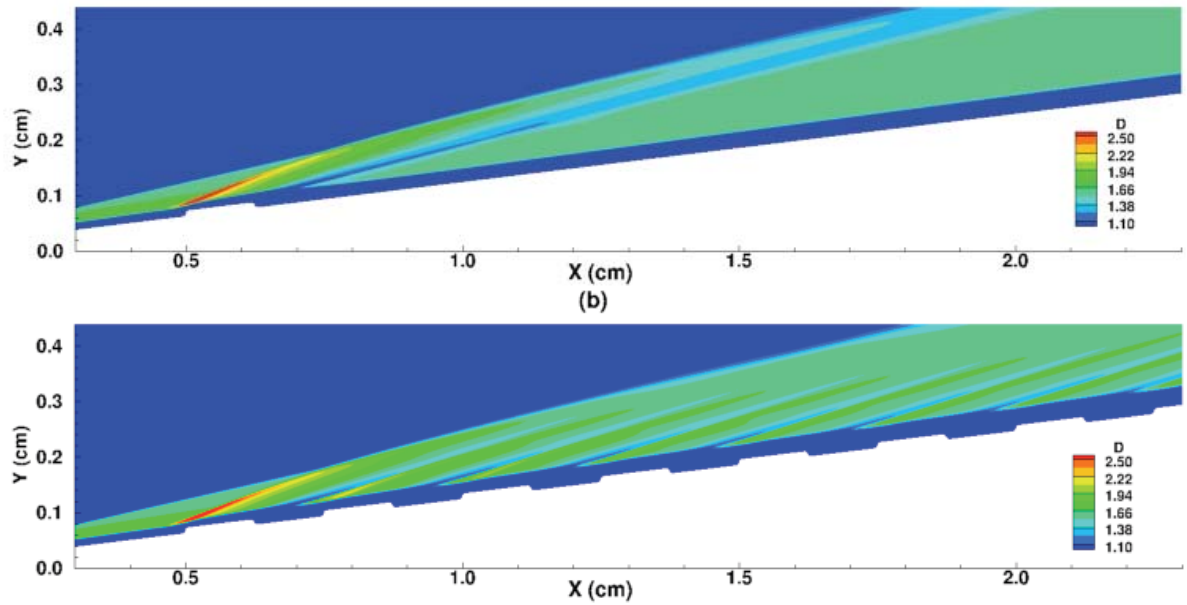
Figure 8: Mean density contours with (a) an isolated roughness, (b) distributed roughness. _h_=0.10 mm, _w_=1.25 mm, _x₀_=5mm.
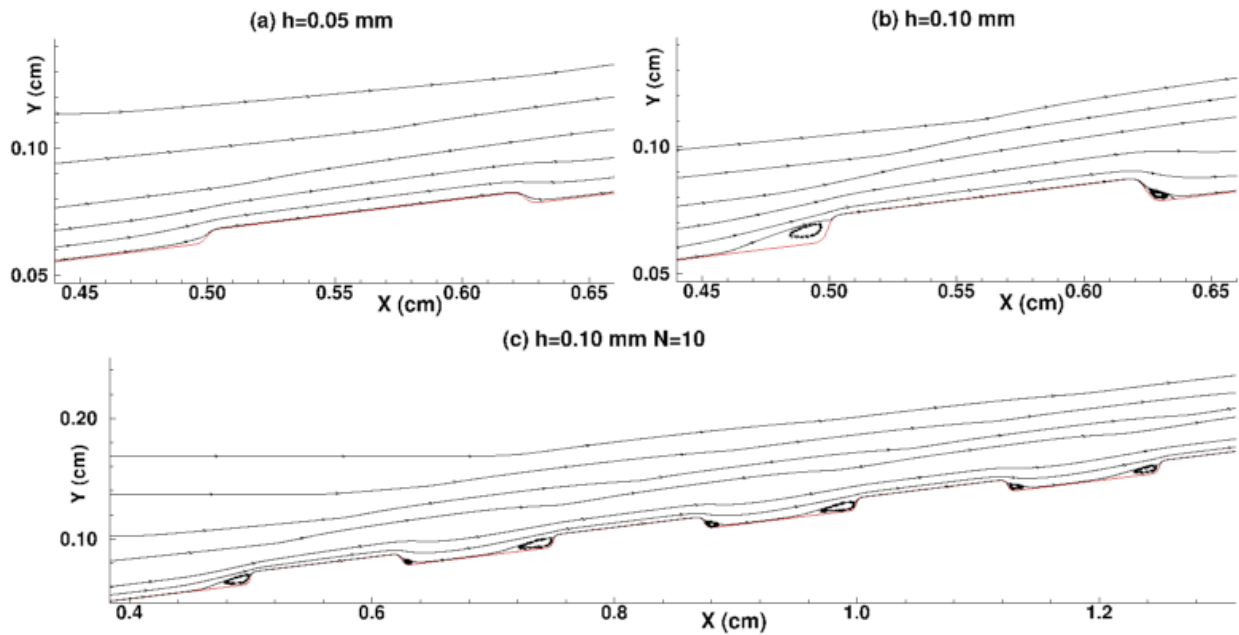
Figure 9: Streamline patterns for the flow over an isolated roughness (a) _h_ = 0.05 mm (b) 0.10 mm, and distributed roughness _h_ = 0.10 mm, N=40. _w_ = 1.25 mm, _x₀_ = 5 mm.
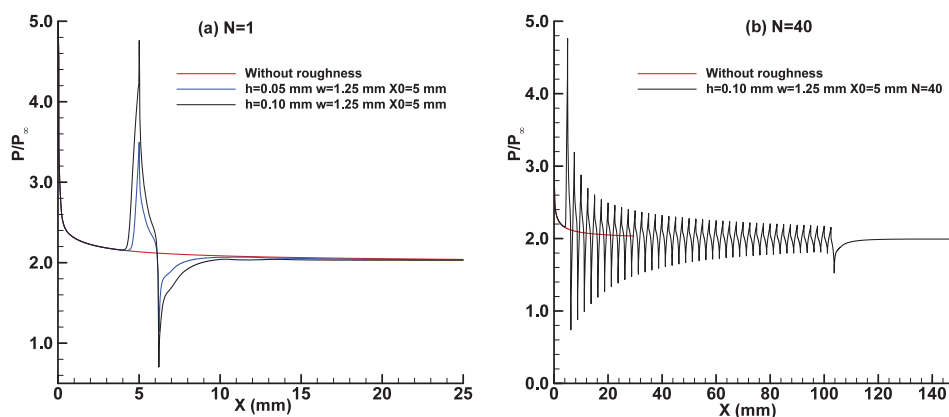
Figure 10: Surface pressure variation with and without roughness. (a) Isolated roughness (b) distributed roughness.
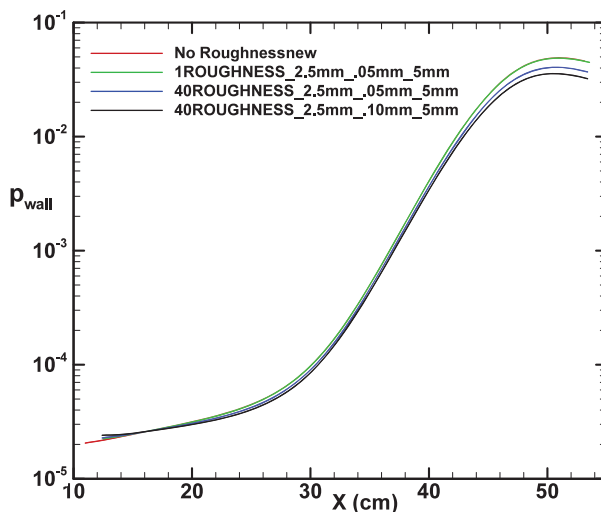
Figure 11: Variation of the amplitude of the pressure variation along the wall computed from linear PSE for different cases.

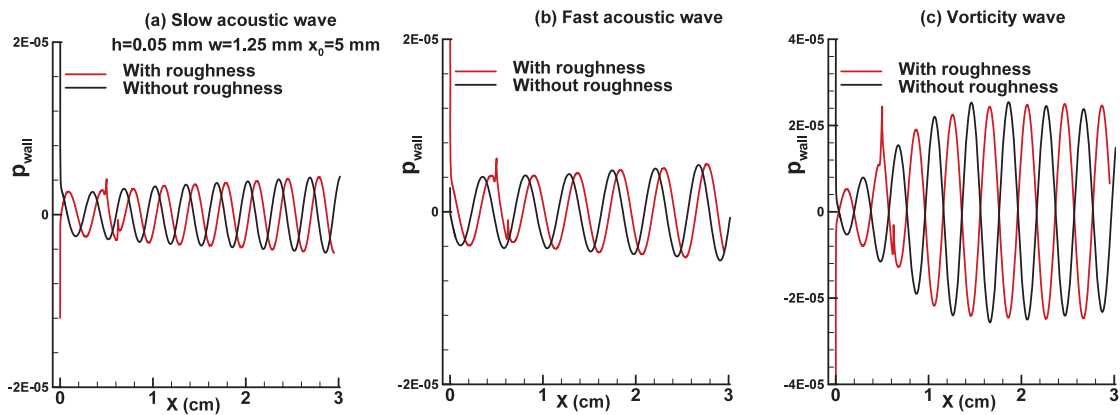**Receptivity of Hypersonic Boundary Layers to**
Distributed Roughness and Acoustic Disturbances
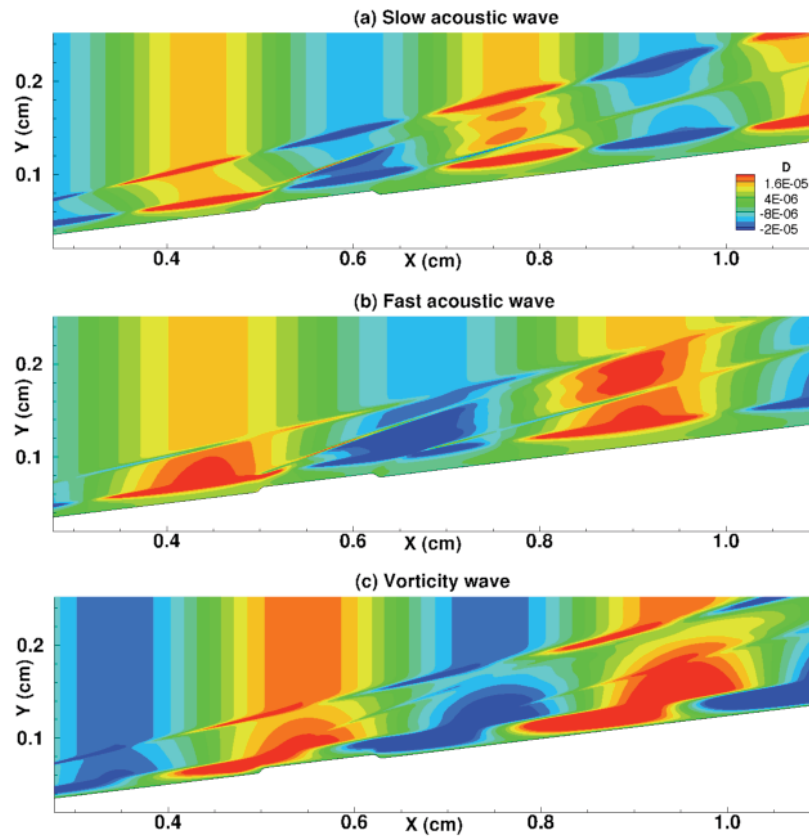
Figure 12: Density fluctuations generated by the interaction of (a) slow, (b) fast acoustic waves and (c) vorticity waves with an isolated roughness. *h=0.05 mm, w=1.25 mm, N=1, F=1.5*10^{-4}*.

Figure 13: Wall pressure fluctuations generated by the interaction of (a) slow (b) fast acoustic waves and (c) vorticity waves with and without roughness. *h=0.05 mm, w=1.25 mm, N=1, F=1.5*10^{-4}*.
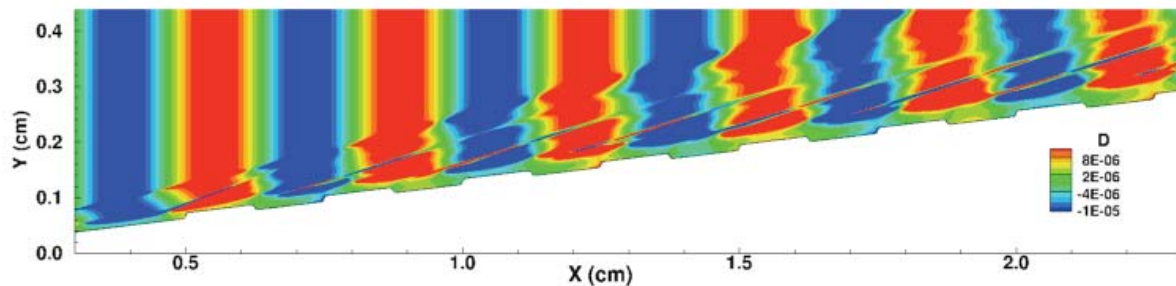
Figure 14: Density fluctuations generated by the interaction of a slow acoustic wave with distributed roughness. *h=0.10 mm, w=1.25 mm, N=40, F=1.5*10^{-4}.*
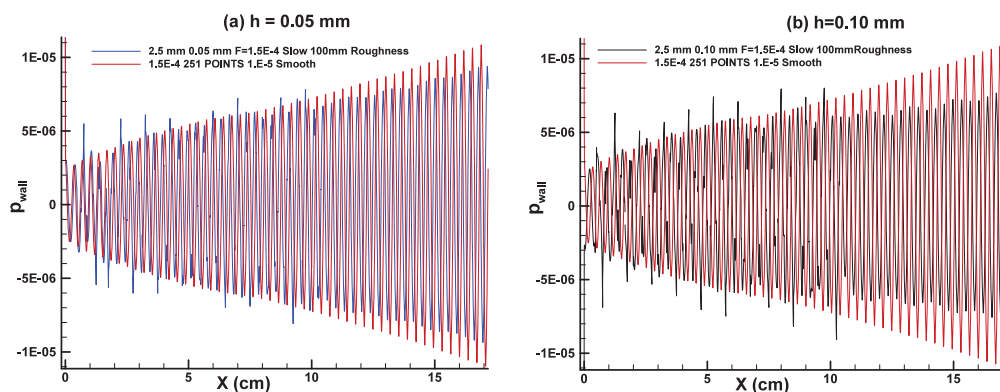

Figure 15: Wall pressure fluctuations generated by the interaction of a slow acoustic wave with distributed roughness. Close to the roughness. *(a) h=0.05 mm (b) h=0.10 mm. w=1.25 mm, N=40, F=1.5*10^{-4}.*
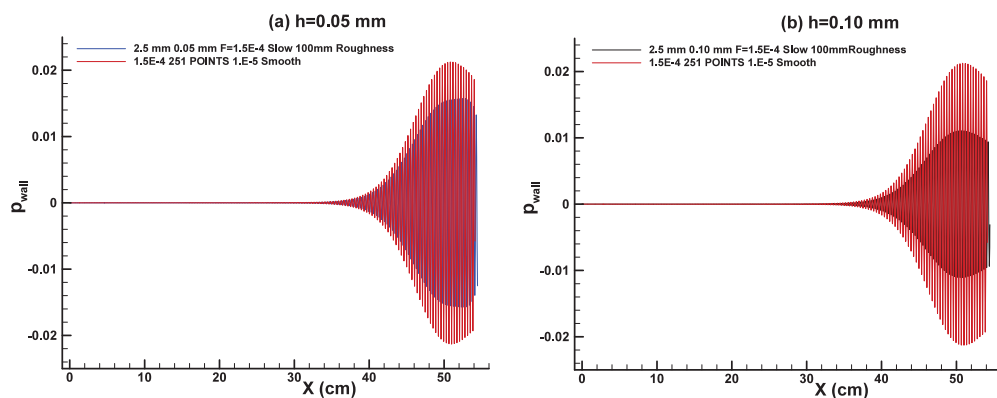

Figure 16: Wall pressure fluctuations generated by the interaction of a slow acoustic wave with distributed roughness. Further downstream. *(a) h=0.05 mm (b) h=0.10 mm. w=1.25 mm, N=40, F=1.5*10^{-4}.*